

DOI: 10.24425/amm.2018.125127

L. MADEJ<sup>\*#</sup>, K. PERZYŃSKI<sup>\*</sup>, M. SKŁADZIEŃ<sup>\*</sup>, M. TKOCZ<sup>\*\*</sup>, M. ROSIAK<sup>\*\*\*</sup>, F. GROSMAN<sup>\*\*</sup>

## APPLICATION OF THE GTN MODEL TO NUMERICAL SIMULATION OF DISTALOY AB SINTERS BEHAVIOUR UNDER COMPLEX LOADING CONDITIONS

The behaviour of porous sinters, during compression and compression with reverse cyclic torsion tests is investigated in the article based on the combination of experimental and numerical techniques. The sinters manufactured from the Distaloy AB powder are examined. First, series of simple uniaxial compression tests were performed on samples with three different porosity volume fractions: 15, 20 and 25%. Obtained data were then used during identification procedure of the Gurson-Tvergaard-Needleman finite element based model, which can capture influence of porosity evolution on plasticity. Finally, the identified Gurson-Tvergaard-Needleman model was validated under complex compression with reverse cyclic torsion conditions and proved its good predictive capabilities. Details on both experimental and numerical investigations are presented within the paper.

*Keywords:* numerical modelling, porous sinters, deformation

### 1. Introduction

Porous sinters in comparison to solid materials have different and often very diversified morphology of microstructure, where the main dissimilarities are associated with presence of discontinuities [1]. From one side, the morphology of porosity strongly depends on the character of metallic powders used during sintering e.g. their shape, dispersion level etc. [2]. On the other side, the morphology is also influenced by a sintering process parameters or applied plastic deformation [3]. In solids final properties of the product are mainly a consequence of the selected material as well as history of plastic deformation. However, in porous sinters, additionally morphological aspects of discontinuities e.g. size, shape, agglomeration, volume fraction play an important role and directly influence final material properties and behaviour. Therefore, from the metal forming operations point of view, all of the above mentioned parameters should be considered during designing of forming process technological chain for sinters.

That is why the overall goal of the present research is evaluation of influence of complex stress states occurring during unconventional forming operation, where the cyclic reverse torsion is superimposed on the uniaxial compression, on porous sinters behaviour. It is expected that such complex deformation state will influence e.g. the material densification process leading to reduction of porosity volume in the final product. Detailed investigation on the matter, usually requires large set of experimental analysis performed with one of the

design of experiment (DoE) approaches. To limit the amount of experimental work and extend the investigation at the same time, numerical models with different levels of complexity can be used [4-6]. However, the crucial aspect in this case is to directly take into account evolution of porosity and its influence on hardening behaviour during deformation. There are various hardening models available in the literature that meet mentioned requirement e.g. coupled pore fluid flow [7], Deshpande and Fleck model [8], Gibson and Ashby model [9-11] or Gurson-Tvergaard-Needleman (GTN) model [12,13]. The latter was selected for the present investigation.

Thus, development and validation of the finite element based, fully coupled GTN model for numerical modelling of complex deformation conditions of sinters is the subject of the work.

### 2. The Gurson-Tvergaard-Needleman model

The Gurson-Tvergaard-Needleman model originates from the research on damage evolution by voids formation during plastic deformation. The model is primarily based on the Gurson work from the 1977 [14] where the yield surface is described as:

$$\phi = \left( \frac{\sigma_i}{\sigma_Y} \right)^2 + 2f \cos h \left( -\frac{3\sigma_m}{2\sigma_Y} \right) - 1 - f^2 = 0 \quad (1)$$

where:  $\sigma_i$  – equivalent stress,  $\sigma_Y$  – yield stress,  $\sigma_m$  – hydrostatic stress,  $f$  – voids volume fraction in the material.

\* AGH UNIVERSITY OF SCIENCE AND TECHNOLOGY, AL. MICKIEWICZA 30, 30-059 KRAKOW, POLAND

\*\* SILESIAAN UNIVERSITY OF TECHNOLOGY, 2A AKADEMICKA STR., 44-100 GLIWICE, POLAND

\*\*\* OPOLE UNIVERSITY OF TECHNOLOGY, 5 S. MIKOLAJCZYKA STR., 45-271 OPOLE, POLAND

# Corresponding author: lmadej@agh.edu.pl

In the following years, Tvergaard and Needleman [15] modified the Gurson equation by adding  $q_1, q_2, q_3$  parameters related to plastic material behaviour and relative density  $f$  of voids:

$$\phi = \left( \frac{\sigma_i}{\sigma_Y} \right)^2 + 2q_1 f \cosh \left( -q_2 \frac{3\sigma_m}{2\sigma_Y} \right) - (1 + q_3 f^2) = 0 \quad (2)$$

where:  $q_i$  – coefficients associated with plastic properties of the material.

In the case when material is fully densified the  $f=0$ , and the GTN model reduces to the classical von Mises plasticity model:

$$\phi = \left( \frac{\sigma_i}{\sigma_Y} \right)^2 \quad (3)$$

The GTN model can then be extended to take into account the varying number of voids during different stages of deformation by defining of a new parameter  $f^*$ :

$$f^* = \begin{cases} f & \text{for } f \leq f_c \\ f_c + \frac{\bar{f}_F - f_c}{f_F - f_c} (f - f_c) & \text{for } f_c < f < f_F \\ \bar{f}_F & \text{for } f \geq f_F \end{cases} \quad (4)$$

where:  $f_c$  – critical volume fraction of voids corresponding to the beginning of their joining,  $f_F$  – critical volume fraction of voids corresponding to the fracture,  $\bar{f}_F$  – parameter describing void's growth rate  $f^*$  that depends on the material related coefficients:

$$\bar{f}_F = \frac{q_1 + \sqrt{q_1^2 - q_3}}{q_3} \quad (5)$$

With this modification, information on initial volume fraction prior deformation, during and after reaching a critical  $f_c$  is taken into account along with the increasing or decreasing number of pores. When the  $f^*$  parameter is taken into account the equation (2) is expressed as:

$$\phi = \left( \frac{\sigma_i}{\sigma_Y} \right)^2 + 2q_1 f^* \cosh \left( -q_2 \frac{3\sigma_m}{2\sigma_Y} \right) - (1 + q_3 f^{*2}) = 0 \quad (6)$$

Despite the fact that the GTN model originated from the damage modelling, it is also often used for numerical simulation of porous sinters. For example in [16] Authors modelled voids propagation in S235JR steel grade. The parameters of the GTN model were identified as  $q_1 = 1.91$ ,  $q_2 = 0.79$ ,  $q_3 = 3.65$ . Interesting applications of the GTN model are also associated with numerical modelling of the pitting corrosion see e.g. [17]. It should also be mentioned that not only metallic materials are being simulated with the GTN model. Other type of materials including biological ones like bones are often modelled with the approach [18].

It have to be pointed out, that no matter the application of the GTN model, in each case, for particular material its parameters have to be properly identified. The identification process primarily requires determining constitutive parameters  $q_1, q_2, q_3$  affecting plasticity. The identification procedure used in the present investigation for the Distaloy AB is described in the following chapter.

### 3. Identification of the GTN model parameters

As mentioned, the most important parameters, which have to be evaluated in the GTN model before numerical modelling are  $q_1, q_2$  and  $q_3$  coefficients. The inverse analysis approach [19] was used in the present investigation for the identification purposes. The procedure is composed of three crucial components: experimental data from the laboratory test, numerical data from the direct problem model of the laboratory test and optimisation algorithm.

To obtained experimental data for the inverse analysis, the standard uniaxial compression test was selected. Three different samples with varying levels of initial porosity volume fraction were considered to cover the wide range of possible material states. Sintors were obtained from the Distaloy AB powder manufactured during the reduction of iron oxides contained in the ore with solid substances. Chemical composition of the powder used for the preparation of sinters is presented in Table 1 [20]. Within the investigation, samples with the following dimensions  $\Phi 15.33/15.73$  mm and three relative volume fractions of pores were obtained  $f_1 = 0.25, f_2 = 0.2$  and  $f_3 = 0.15$ .

TABLE 1

Chemical composition of the powder used during the investigation

Chemical Element	Type of powder
	Distaloy AB
	Fraction %
H <sub>2</sub> loss	0.08
C	<0.01
Ni	1.78
Cu	1.53
Mo	0.51
Fe	The rest

The initial volume fraction of pores was confirmed by the hydrostatic weighting procedure according to the DIN 30911-3. Finally, the cylindrical samples were subjected to uniaxial compression at the universal machine for testing materials under complex loading conditions (Fig. 1), with the height reduction equal to 10 mm.

Set of six samples with three different levels of porosity were investigated to obtain repeatable results of measured load-displacement curves as presented in Fig. 2.

During the second stage of the identification procedure, the direct problem model replicating experimental compression setup was developed within the commercial Abaqus software. The sample was considered as deformable and described by a fully thermo-mechanical model that takes into account influence of deformation heating on material flow [21]. The thermal properties of the investigated material were taken from [22]. For simplicity the upper and lower dies were considered as discrete rigid parts.

All numerical models of subsequent parts were finally combined in the assembly module and boundary conditions replicating laboratory compression tests were defined as seen



Fig. 1. Universal machine for testing materials under complex loading conditions

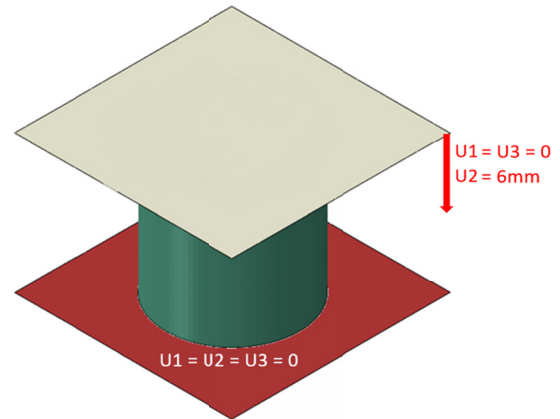


Fig. 3. Model assembly with the applied boundary conditions

TABLE 2

Identified parameters of the GTN model for the Distaloy AB.

Porous Volume Fraction	$q_1$	$q_2$	$q_3$
15%, 20%, 25%	2.2	0.3	4.84

The agreement between measured and calculated loads for the identified parameters is presented in Fig. 4.

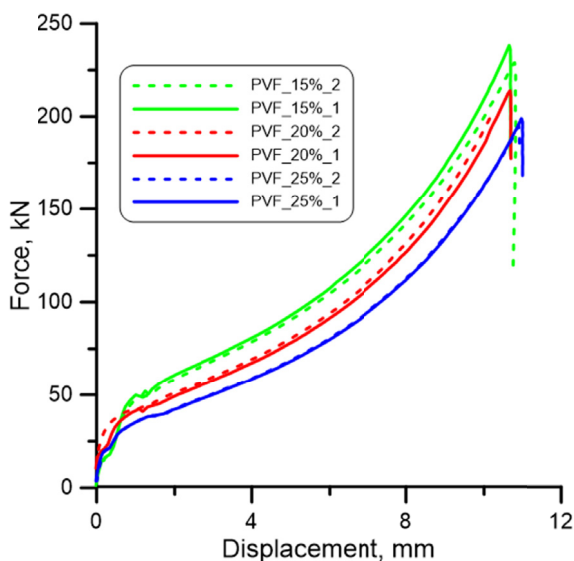


Fig. 2. Load-displacement curves after compression tests for samples with three different porosity volume fractions (PVF)

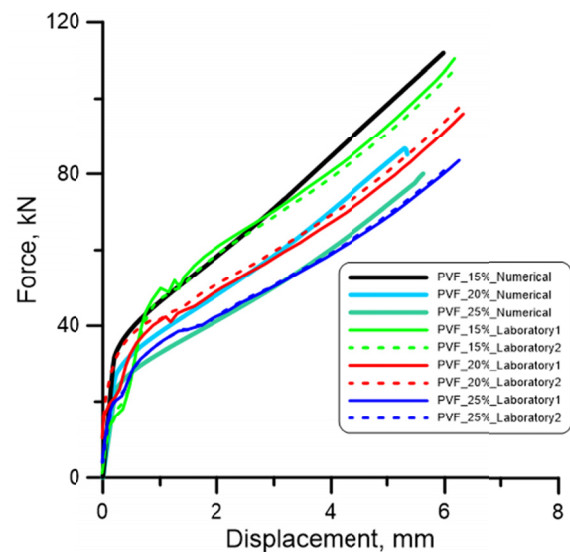


Fig. 4. Comparison of load-displacement curves from compression test obtained from experimental and inverse analysis

in Fig. 3. The lower die was fully constrained while upper die was displaced in OY direction by 6 mm to limit computational time during the inverse analysis.

The 92000 of 8 node linear brick, reduced integration and hourglass controlled elements (C3D8R) were selected for the discretization purposes.

The GTN coefficients  $q_1, q_2, q_3$  were then identified during the inverse analysis based on simplex optimisation method [19,23] by minimising the goal function defined as a square root difference between measured and calculated loads. After, series of optimisation stages a set of model parameters was obtained as presented in Table 2.

The identified GTN model, was then validated during numerical simulations of more complicated deformation process involving superposition of cyclic reverse torsion and compression tests.

#### 4. Validation of the GTN model parameters

The compression with reverse cyclic torsion test was selected for validation purposes to prove that the developed GTN model properly describe material behaviour under such complex stress state. Laboratory tests were again realized with universal

machine for testing materials under complex loading conditions where the following parameters can be setup:

- rotation angle  $\alpha$  – the upper die rotates in the  $x$  and  $y$  plane with the frequency  $f$ ,
- rotation frequency  $f$  – defines the number of rotations per second,
- compression velocity  $v$ .

To properly transfer the reverse torsion movement of the die, specific shaped sample and dies were used. The sample presented in Fig. 5 was used during the investigation.

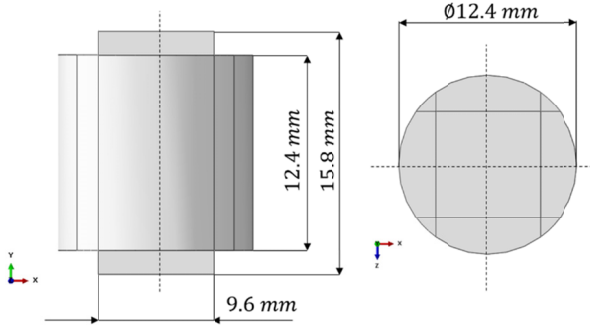


Fig. 5. Sample geometry used during the investigation

Samples were located between two properly shaped dies as shown in Fig. 6.

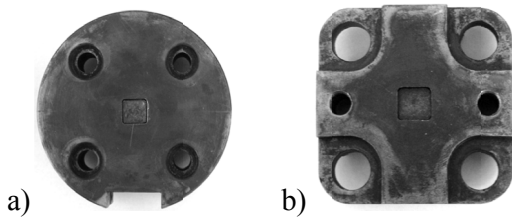


Fig. 6. a) Upper die, b) lower die

During the laboratory tests the lower die rotated up to  $6^\circ$  in both directions with frequency 0.5 Hz. Press velocity was constant and equal 0.09 mm/s. The same process conditions were used for three different initial volume fractions of porosity in the investigated samples. Obtained loads as a function of time are presented in Fig. 7.

The investigated deformation process was then recreated within the numerical finite element software Abaqus. In order to simulate compression test with reverse torsion movement of the die appropriate boundary conditions were defined. The reverse torsion parameters were controlled by the periodic amplitude equation:

$$a = A_0 + \sum_{n=1}^N [A_n \cos n\omega(t-t_0) + B_n \sin n\omega(t-t_0)]$$

$$\begin{aligned} & \text{for } t \geq t_0 \\ & a = A_0 \text{ for } t < t_0 \end{aligned} \quad (7)$$

where:  $A_0$  – initial amplitude,  $N$  – number of steps,  $n = 1, 2, \dots, N$  – actual step,  $\omega$  – angular frequency,  $t_0$  – time at which the amplitude starts to operate,  $A_n, B_n$  – user-defined constants.

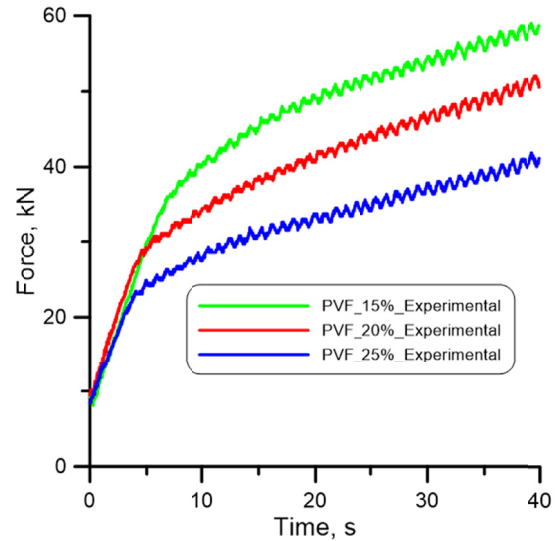


Fig. 7. Load-time curves from compression with reverse cyclic torsion test

Illustration of the applied amplitude with respect to process simulation time is presented in Fig. 8.

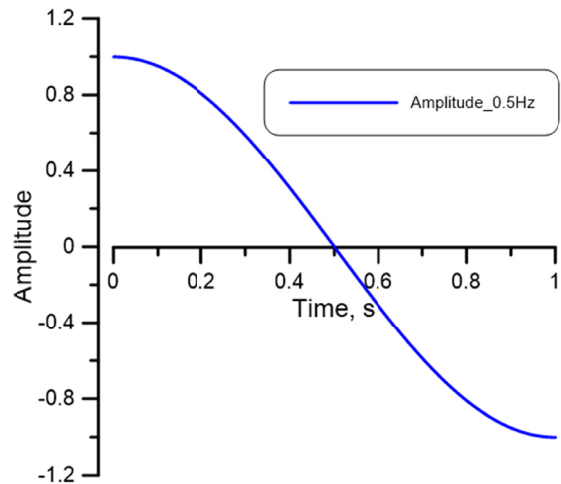


Fig. 8. Amplitude applied to recreate reverse torsion movement of the upper tool in the finite element software

Again 92000 of 8 node linear brick, reduced integration and hourglass controlled elements (C3D8R) were selected for the discretization purposes. Additionally, to increase the predictive capabilities of the model the ALE (Adaptive Lagrangian-Eulerian Mesh Controls) algorithm was used as the sample undergoes significant deformation [24]. In the Lagrange method, mesh nodes move exactly with the material points in which they were created. The mesh is locally deformed at high strains what leads to significant degeneration of the FE elements and lack of convergence of the numerical solution. Using the Euler method, nodes remain at the locations where they were created and do not depend on material movement. The created mesh does not change, its nodes and elements remain as in the initial layout. The combination of these two types of meshes creates a model in which the mesh is associated with the material only where

it is necessary, the movement of the mesh and material can be then independent.

Developed model includes also temperature changes as a result of heat generation induced by deformation. With the presented model a fully coupled thermo-mechanical analysis was performed. Time of the calculation was set as 40 s what

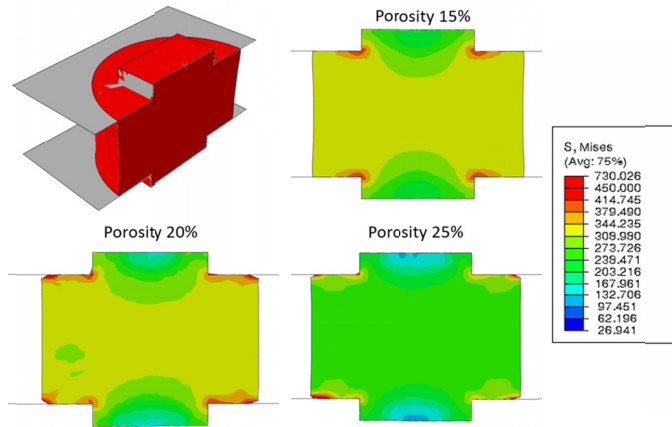


Fig. 9. Equivalent stress distribution after compression with reverse cyclic torsion test

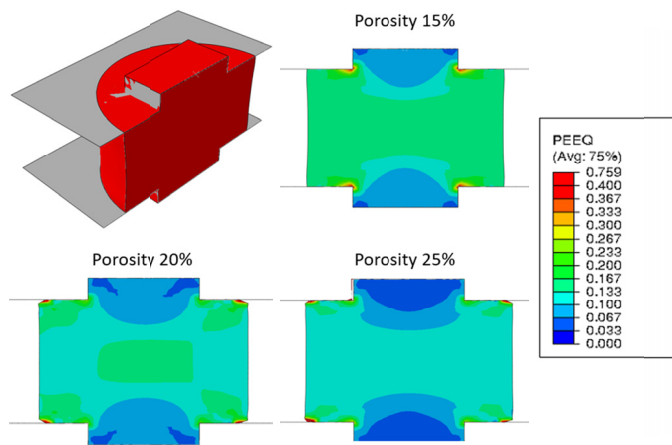


Fig. 10. Equivalent plastic strain distribution after compression with reverse cyclic torsion test

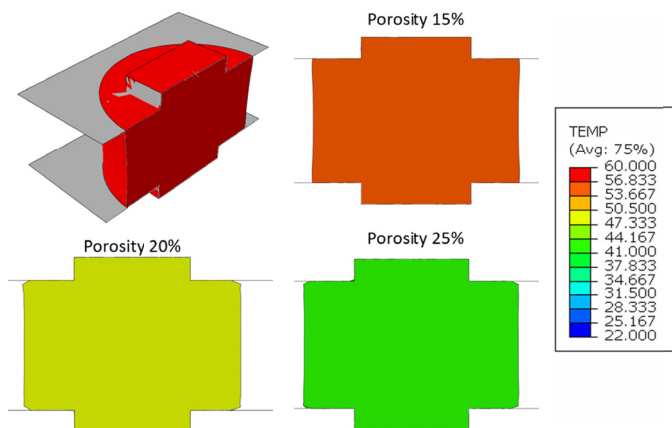


Fig. 11. Temperature distribution after compression with reverse cyclic torsion test

corresponds with deformation of 25%. The parameters from Table 2 were used to validate the predictive capabilities of the identified GTN model. Examples of obtained results are shown in Fig. 9-11.

Comparison of the experimentally measured and calculated loads by the GTN model are presented in Fig. 12.

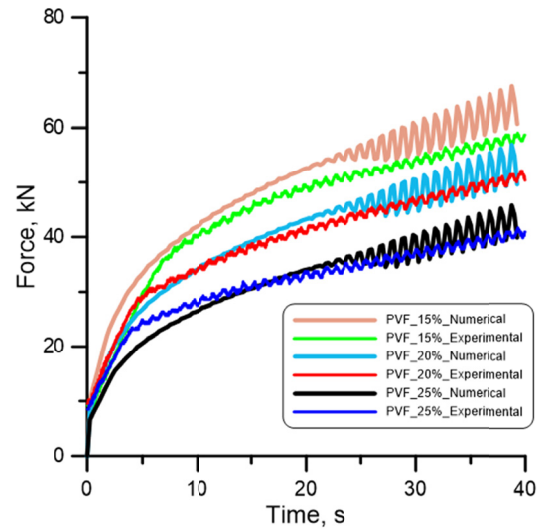


Fig. 12. Comparison of load-time curves from compression with reverse cyclic torsion test obtained from experimental and numerical analysis

As seen in Fig. 12, the model predictions for the three different samples with increasing initial porosity level agree well with the experimental observations. However, at the later stages of deformation some clearly pronounced oscillations, higher than in the experimental measurements, appear at the load curves in all three case studies. Most probably over time, the contact surface between the tool and the sample in numerical simulation increases slightly faster than in experimental investigation, contributing to the increase of torque. Nevertheless it can be concluded, that the developed model can be used not only to simulate simple deformation conditions, but also sinters subjected to complex loading paths. The model will be used during further research to investigate material behaviour during compression with cyclic horizontal reverse shearing.

### 5. Conclusions

- Based on the presented research it can be concluded that:
- GTN model parameters can be properly identified based on conventional compression test performed for a set of samples with different porosity volume fractions.
  - GTN model can properly capture sinters behaviour under complex loading paths. Load reduction during the compression with cyclic reverse torsion in comparison to conventional compression is clearly visible.
  - Due to mesh degeneration, occurring especially when cyclic reverse torsion is superimposed on the compression, the ALE technique should be used during simulation.

- Combination of the reverse torsion and compression lead to uniform equivalent strain distribution across the sample what positively influences uniform reduction of the porosity.

#### Acknowledgments

Financial assistance provided by the National Science Centre under the 2014/15/B/ST8/00086 project is gratefully acknowledged. This research was supported in part by PLGrid Infrastructure.

#### References

- [1] A. Falkowska, A. Seweryn, A. Tomczyk, *Int. J. Fat.* **111**, 161-176 (2018).
- [2] W.S.W. Harun, M.S.I.N. Kamariah, N. Muhamad, S.A.C. Ghani, F. Ahmad, Z. Mohamed, *Powder Technol.* **327**, 128-151 (2018).
- [3] M. Rosiak, J. Napiórkowski, *MATEC Web of Conferences* **94** (2017).
- [4] A. Salvadori, S. Lee, A. Gillman, K. Matouš, C. Shuck, A. Mukasyan, M.T. Beason, I.E. Gunduz, S.F. Son, *Mech. of Mat.* **112**, 56-70 (2017).
- [5] A. Kurzawa, D. Pyka, J. Pach, K. Jamroziak, M. Bocian, *Proc. Eng.* **199**, 1495-1500 (2017).
- [6] K. Matouš, M.G.D. Geers, V.G. Kouznetsova, A. Gillman, *J. Comput. Phys.* **330**, 192-220 (2017).
- [7] W. Sobieski, *Tech. Sci.* **13**, 256-265 (2010).
- [8] S.T. Szyniszewski, B.H. Smith, J.F. Hajjar, B.W. Schafer, S.R. Arwade, *Mater. Des.* **54**, 1083-1094 (2014).
- [9] Q. Sawei, Z. Xinna, H. Qingxian, D. Renjun, J. Yan, H. Yuebo, *Rare Met. Mat. and Eng.* **44**, 2670-2676 (2015).
- [10] H. Mehboob, F. Tarlochan, A. Mehboob, S.-H. Chang, *Mater. Des.* **149**, 101-112 (2018).
- [11] W. Yan, J. Berthe, C. Wen, *Mater. Des.* **32**, 1776-1782 (2011).
- [12] T. Ueda, L. Helfen, T.F. Morgeneyer, *Acta. Mater.* **78**, 254-270 (2014).
- [13] Y. Chen, C. Zhang, C. Varé, *Comp. Mater. Sci.* **128**, 229-235 (2017).
- [14] A.L. Gurson, *J. Eng. Mater. Technol.* **99** (1977).
- [15] V. Tvergaard, A. Needleman, *Acta Metall.* **32**, 157-169 (1984).
- [16] P. Kossakowski, *Roads and Bridges* **11**, 295-310 (2012).
- [17] V. Vijayaraghavan, A. Garg, L. Gao, R. Vijayaraghavan, *Metals (Basel)* **7**, 83 (2017).
- [18] P.J. Sulich, *Czasopismo Techniczne. Mechanika* **109**, 293-309 (2012).
- [19] M. Pietrzyk, Ł. Madej, Ł. Rauch, D. Szeliga, *Computational Materials Engineering: Achieving High Accuracy and Efficiency*, Elsevier, (2015).
- [20] M. Rosiak, *Mechanik* **11**, 1736-1737 (2016).
- [21] H. Seli, M. Awang, A.I.M. Ismail, E. Rachman, Z.A. Ahmad, *Mat. Res.* **16**, 453-467 (2012).
- [22] H.R. Shanks, A.H. Klein, G.C. Danielson, *J. Appl. Phys.* **38**, 2885-2892 (1967).
- [23] D. Szeliga, J. Gawad, M. Pietrzyk, *Comput. Methods. Appl. Mech. Eng.* **195**, 6778-6798 (2006).
- [24] B.T. Helenbrook, J. Hrdina, *Comput. Fluids* **167**, 40-50 (2018).